Hybrid MHD-Gyrokinetic codes: extended models, new implementations and forthcoming applications

G. Vlad, S. Briguglio, G. Fogaccia, F. Zonca

Associazione EURATOM-ENEA, CR ENEA-Frascati, Via E. Fermi 45, 00044 Frascati, (Rome) Italy

e-mail contact of main author: gregorio.vlad@enea.it

Abstract. The hybrid MHD-Gyrokinetic model has been proven to be very successful in describing the coupling between Alfvén waves and energetic particles and their mutual interaction in toroidal devices. HMGC, the nonlinear MHD-Gyrokinetic code originally developed at the Frascati laboratories, is being currently extended to include new physics. In this paper we will present the first simulations of an electron fishbone mode using the extended HMGC code. We will also present some benchmarks of the new hybrid code HYMAGYC (linear resistive MHD in general curvilinear geometry plus fully nonlinear gyrokinetic description, $k_\perp \rho_H \sim 1$, of the energetic particles) with the results obtained by HMGC and an analytical expression of the energetic particle response.

1. Introduction

The hybrid MHD-Gyrokinetic model [1] has been proven to be very successful in describing the coupling between Alfvén waves and energetic particles and their mutual interaction in toroidal devices [2, 3, 4, 5, 6, 7, 8, 9, 10, 11]. HMGC [2], the nonlinear MHD-Gyrokinetic code originally developed at the Frascati laboratories, has been applied to case studies of energetic particle driven modes (such as, e.g., TAEs and EPMs [3, 4, 5]), but also to analyses of experimentally observed modes in existing devices (JT-60U [12], DIII-D [13]) and forthcoming (ITER [6, 14]) or proposed (FAST [15]) burning plasmas experiments. The simple physical model, originally used in HMGC ($O(\epsilon^3)$ nonlinear reduced MHD equations, circular shifted magnetic surface equilibrium, zero bulk plasma pressure, and drift-kinetic fast ions), has been recently extended to include new physics, which are currently under implementation and/or benchmarking [16]. These extensions include both thermal ion compressibility and diamagnetic effects, in order to account for thermal ion collisionless response to low-frequency Alfvénic modes driven by energetic particles (e.g., KBAEs), and finite parallel electric field due to parallel thermal electron pressure gradient, which enters the parallel Ohm's law and generalizes it, accounting for the kinetic thermal plasma response. Moreover, HMGC is now able to treat two independent particle populations kinetically, assuming different equilibrium distribution functions (as, e.g., bulk ions, energetic particles accelerated by NB, IRCH, fusion generated alpha particles, etc.). Applications of the extended HMGC include, e.g., kinetic thermal ion effects on Alfvénic fluctuations, electron and ion fishbones, KBAEs, fast ion driven GAMs, EPMs in burning plasma experiments with multiple fast ion species (as in the case of FAST [15]). The HMGC code also participates to several benchmark activities within the ITPA Energetic Particle group [17] and the SciDAC GSEP collaboration [18]. On a separate ground, the new hybrid code HYMAGYC [19] (linear resistive MHD in general curvilinear geometry plus fully nonlinear gyrokinetic description, $k_\perp \rho_H \sim 1$, of the energetic particles) is under testing: several benchmarks between HYMAGYC and HMGC in overlapping regimes of validity and comparison with analytically computed particle responses are underway. In the following sections, the first results obtained in simulating an electron fishbone mode using the extended HMGC code (see Sect. 2), and a detailed benchmark of the gyrokinetic model of HYMAGYC both with analytical expressions and HMGC results for the particles responses (see Sect. 3) will be presented.

2. Electron fishbone simulations using the extended version of HMGC

Internal kink instabilities exhibiting fishbone like nature have been observed in a variety of experiments where a high energy electron population was present (among others, DIII-D [20], Compass-D [21], HL-1M [22], FTU [23] and Tore Supra [24]). The relevance of the electron fishbones is primarily related to the fact that suprathermal electrons are characterized by relatively small width orbits, when compared with those of fast ions, similarly to the case of alpha particles in burning plasmas: thus, electron fishbones offer the opportunity to study the coupling between energetic particles and MHD like modes in burning plasma relevant conditions even in present machines. In fact, precession resonance depends on energy, not mass; meanwhile, suprathermal electron transport perpendicular to **B** caused by fishbones can reflect some properties of fluctuation induced transport of fusion alphas due to precession resonance.

In the present study we will refer to the typical parameters of the FTU machine, where electron fishbones appearance has occurred in Lower Hybrid heated discharges. However, in these preliminary studies we will not refer to a specific FTU discharge. To this aim, we have used the recently extended HMGC code [16]. The FTU-like equilibrium corresponds to a torus with circular shape cross section, with an inverse aspect ratio $\epsilon \equiv a/R_0 \approx 0.35$ (with a and R_0 the minor and major radius, respectively). The safety factor profile has been assumed slightly reversed, with $q_0 \approx 1.2$, $q_{\min} \approx 1.05$ at $r_{q_{\min}}/a \approx 0.3$, and $q_a \approx 3.1$. Reference magnetic field $B_T = 5$T, deuterium bulk plasma with on-axis density $n_{i0} = 1 \times 10^{20} m^{-3}$ and a profile $n_i(\psi)/n_{i0} = (1 - \psi_{\mathrm{norm}})^{1/2}$, on-axis ion temperature $T_{i0} = 2$ keV and radial profile $T_i(\psi)/T_{i0} = (1 - \psi_{\mathrm{norm}})$ have been assumed; here ψ_{norm} is the normalized poloidal flux (being $\psi_{\mathrm{norm}} = 0$ on-axis and $\psi_{\mathrm{norm}} = 1$ at the plasma boundary).

The particle populations treated kinetically will be the energetic electrons, described by a strongly anisotropic Maxwellian distribution function, and the bulk ions, described by an isotropic Maxwellian. In this way, both resonant excitation by suprathermal electrons as well as thermal ion Landau damping and finite compressibility are accounted for.

As to energetic electrons, particles have been loaded accordingly to the following $f_{\mathrm{electrons}}$ distribution function:

$$f_{\mathrm{electrons}} \quad \propto \quad \frac{\hat{n}_{Ee}(\psi)}{\tau_{Ee}(\psi)^{3/2}} \Theta(\alpha; \alpha_0, \Delta) e^{-E/T_{Ee}(\psi)} \equiv \frac{\hat{n}_{Ee}(\psi)}{\tau_{Ee}(\psi)^{3/2}} \hat{f}_{\mathrm{electrons}} \tag{1}$$

$$\Theta(\alpha; \alpha_0, \Delta) \quad \equiv \quad \frac{4}{\Delta\sqrt{\pi}} \frac{\exp\left[-\left(\frac{\cos\alpha - \cos\alpha_0}{\Delta}\right)^2\right]}{\mathrm{erf}\left(\frac{1 - \cos\alpha_0}{\Delta}\right) + \mathrm{erf}\left(\frac{1 + \cos\alpha_0}{\Delta}\right)}, \tag{2}$$

$$E = \frac{1}{2} m_e u^2 + \mu\Omega_{ce}, \quad \cos\alpha \equiv \frac{u}{\sqrt{2E/m_e}}, \quad \sin^2\alpha \equiv \frac{\mu\Omega_{ce}}{E}, \tag{3}$$

with E the energy, $\hat{n}_{Ee}(\psi)$ the radial density profile normalized to the on-axis value n_{Ee0}, $T_{Ee}(\psi)$ the temperature and $\tau_{Ee}(\psi) \equiv T_{Ee}(\psi)/T_{Ee0}$ the radial temperature profile normalized to the on-axis value T_{Ee0}, u the parallel (to the equilibrium magnetic field) velocity, μ the conserved magnetic moment, α the pitch angle of the energetic electrons, $\Theta(\alpha; \alpha_0, \Delta)$ representing the anisotropy of the distribution function and $\Omega_{ce} = eB/(m_e c)$ with e, m_e the (absolute value of) charge and mass of electrons, respectively, and B the (local) equilibrium magnetic field. In the code, the parallel velocity is normalized to the on-axis energetic electron thermal velocity $\hat{u} \equiv u/v_{th0}$, with $v_{th0} = \sqrt{T_{Ee0}/m_e}$, and the magnetic moment is normalized as

$\hat{\mu} \equiv \mu\Omega_{ce0}/T_{Ee0}$, with Ω_{ce0} the on-axis cyclotron frequency. The values of $\cos\alpha_0 = 0$ and $\Delta = 0.1$ have been considered (thus assuming the perpendicular temperature much higher than the parallel one). In Figs. *1*. the anisotropic part of the electron distribution function $\hat{f}_{\text{electrons}}$ in the normalized space $(\hat{\mu}, \hat{u})$ and the radial (ψ) dependence of the energetic electrons density are shown (the radial position of the maximum gradient of the energetic electrons density is somewhat internal but close to the minimum q position $r_{q_{\min}}$). Energetic electrons are characterized by uniform temperature $T_{Ee} = T_{Ee0} = 50$ keV.
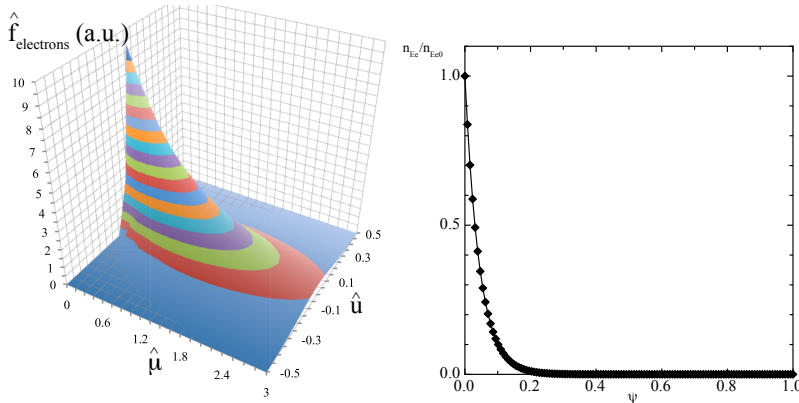

FIG. *1*.: $\hat{f}_{\text{electrons}}$ function in the plane $(\hat{\mu}, \hat{u})$ (left), and normalized energetic electrons density profile vs. the normalized poloidal flux function ψ (right).

Note that for these preliminary studies on electron fishbones on-axis peaked energetic electron density has been assumed, whereas, usually, LH experiments on FTU have typical off-axis peaked profiles.

Energetic electrons will be characterized, generally speaking, by much higher velocities than the ones of the bulk ions, which also will be treated kinetically to describe properly ion Landau damping and thermal ion compression; thus, the problem of properly choosing the time step for the simulation arises. In the actual version of HMGC a time step sub-cycling algorithm has been implemented, such that, at fixed time step on which the field solver advances the solution, each particle in the gyrokinetic module is able to sub-divide the time step in order to properly integrate the equations of motion. Accordingly, the fields are linearly interpolated in time during the sub-cycling. As the accuracy condition requires very different sub-cycling levels, depending on the velocity magnitude and the closeness to the magnetic axis, this individual sub-cycling algorithm reveals to be fairly efficient.

It has to be noted that the suprathermal electron distribution function, as previously assigned, is given in terms of variables (E, α, ψ), which are not all constant of the unperturbed motion. Thus, one can expect that the distribution function relaxes in time. To prevent this to occur in the following simulations, the ∇B drift contribution to the source term in the equation that evolves the weight of the particles has been neglected, thus forcing the equilibrium distribution function to be constant in time.

A simulation, showing an unstable mode driven by the energetic electrons, is reported in Fig. *2*. (left), where the toroidal mode number considered is $n = 1$, and the poloidal Fourier components retained are $m = 1, ..., 4$. The mode exists only if a threshold in n_{Ee0}/n_{i0} is exceeded, which, for this particular equilibrium, is $n_{Ee0}/n_{i0} \approx 0.055$. A very clear growing mode, with
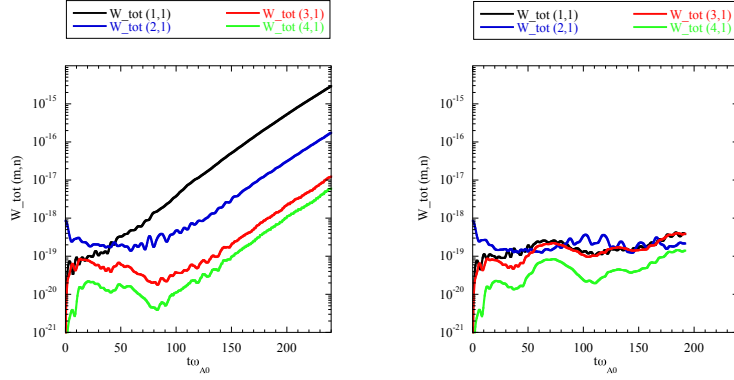
FIG. 2.: Energetic electron driven mode: total energy content in the different Fourier components used in the simulation (left). No unstable mode is observed (right) in a similar simulation in which, artificially, the mirroring term in the energetic electron equations of motion has been switched off.

the characteristics of a $n = 1$ internal kink is observed, with a displacement function which is quite diffused (different from the classic, $m = 1$ "step function"), because of the weakly reversed shear inside the q_{min} surface used in the simulation. This can be seen in Fig. 3., where the poloidal structure of the eigenfunction is shown together with the power spectrum of the electrostatic component of the fluctuating electromagnetic fields. Note that the mode rotates counterclockwise, i.e. in the direction of the diamagnetic velocity of the suprathermal electrons, with a real frequency of $\omega/\omega_{A0} = -0.0815$ and a growth rate $\gamma/\omega_{A0} = 0.024$, ω_{A0} being the on-axis Alfvén frequency, and, thus, $\gamma/|\omega| \approx 0.29$. A first evidence that the mode shown in Fig. 2. (left) is actually an e-fishbone, can be obtained by artificially switching off the mirroring term in the equations of motion of the energetic electrons, thus suppressing the contribution of trapped electrons: this is shown in Fig. 2. (right), where the energy content of the different Fourier components are plotted vs. time, showing that the system, in this case, is stable.
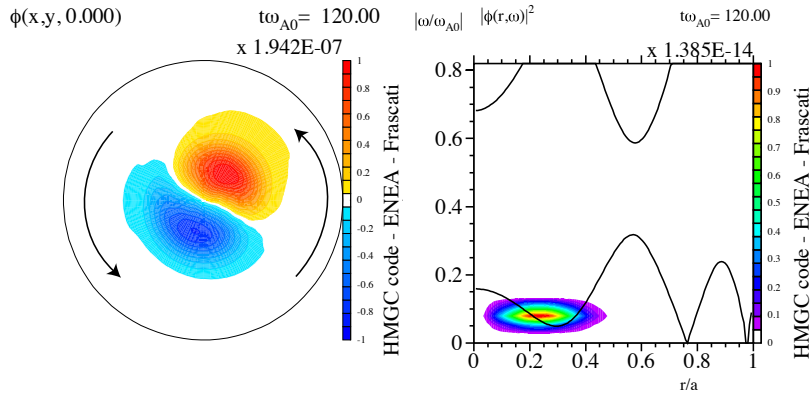

FIG. 3.: Poloidal structure of the energetic electrons driven mode (electrostatic component of the fluctuating electromagnetic field, left), and its power spectrum (right); the black curves represent the Alfvén continuous spectrum.

To better clarify the dynamics of energetic particles, the power transfer from the energetic electrons to the wave during the linear growth of the mode is shown in Fig. 4. (left) versus $\hat{\mu}$ and $\hat{u}$, at the radial position where the power exchange is maximum ($r/a \approx 0.15$). Figure 4. (right) shows

the analogous quantity for the thermal ions. Trapped energetic electrons are clearly driving the wave, whereas mainly the counterpassing bulk ions contribute to Landau damping. Note that, in Fig. *4.*, each particle contribution is referred to the value of $\hat{u}$ of that particle when crossing the equatorial plane.
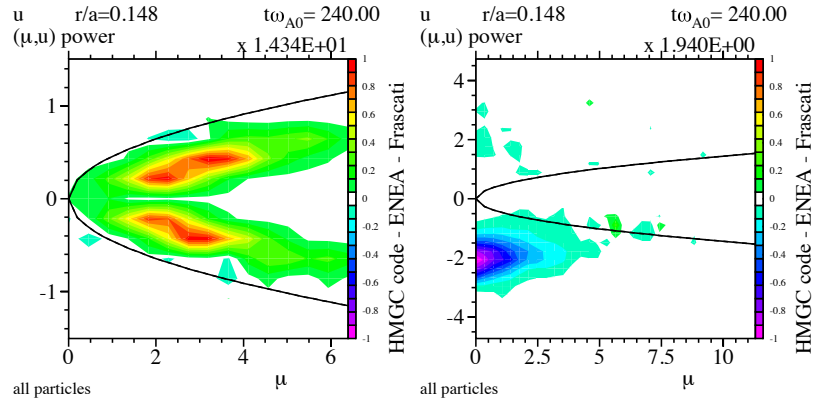

FIG. 4.: Power exchange in the $(\hat{\mu}, \hat{u})$ space between, respectively, suprathermal electrons (left) and the bulk ions (right) and the wave at the radial position where the power exchange is maximum ($r/a \approx 0.15$) (violet color code corresponds to maximum damping, red to maximum drive). The black curves correspond to the trapped/passing region boundary. Note that electrons and ions velocity space variables normalizations are different.

The details of the power exchange between the energetic electrons and the wave are shown in Fig. *5.*, where the contribution of the counterpassing, the trapped and the copassing fractions of the energetic electrons are shown separately: the trapped populations clearly give the major contribution to the total power exchange (see also with Fig. *4.* (left)), suggesting that the resonance of the mode occurs with the trapped electron precession motion, whereas the counterpassing and copassing fractions give a small damping. This is consistent with the fact that barely trapped/circulating electrons are characterized by precession reversal [25].
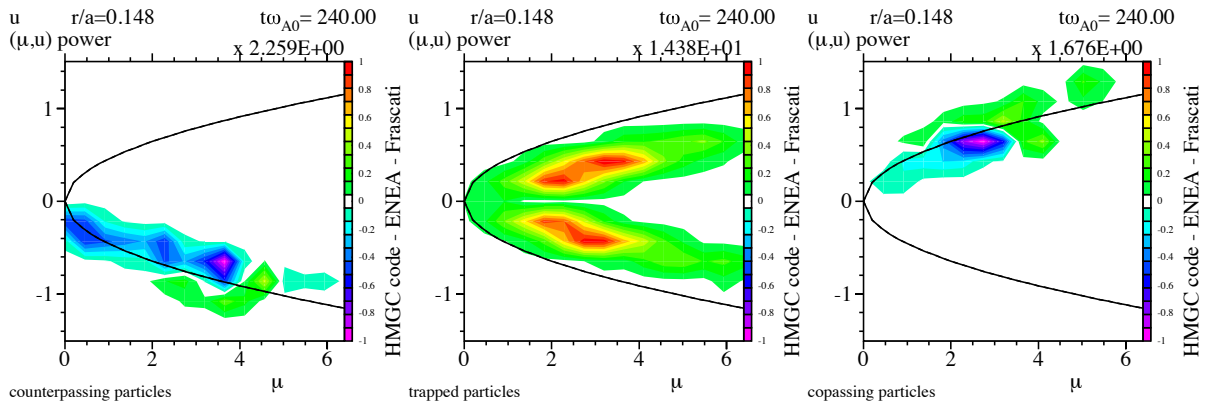

FIG. 5.: Power exchange in the $(\hat{\mu}, \hat{u})$ space between the energetic electrons and the wave: counterpassing (left), trapped (centre) and copassing (right) fractions, respectively. Note that the color code scale is relative to each plot.

While performing a numerical simulation, the HMGC code can also be used to evolve a set of test particles; the generalized coordinates of such particles are stored in time, and can be used, after the simulation has finished, to compute a variety of single particle features. In this case, we are interested in analyzing the single particle frequencies, namely, the precession and bounce

frequencies. To this purpose, a set of test particles has been initialized at the radial location where the power exchange is maximized, sampling the same region of space $(\hat{\mu}, \hat{u})$ used for the power exchange plots (see Figs. *4.*, *5.*).

The bounce frequencies are always much larger, in absolute value, than the mode frequency and, as expected, the precession frequencies of the trapped test particles fall in the range of the mode frequency. In Fig. *6.* the power exchange between the trapped energetic electrons and the wave is shown together with a family of curves describing the resonance conditions $\omega_{\text{precession}} - \omega = 0$, for several values of ω. As it is clear from the Figure, the maximum power exchange is between the curves defined by $\omega/\omega_{A0} = -0.05$ (thick, black curves) and $\omega/\omega_{A0} = -0.10$ (red curves), in good agreement with the mode frequency $\omega_{\text{mode}}/\omega_{A0} = -0.0815$ obtained from the simulation.
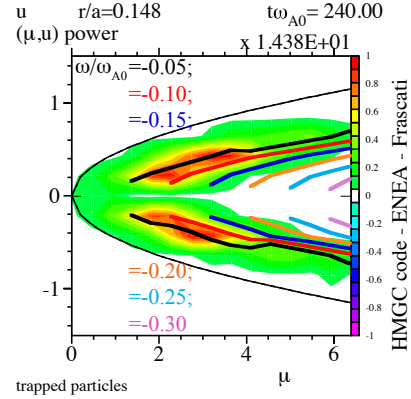

FIG. 6.: Power exchange, in the $(\hat{\mu}, \hat{u})$ space, between the trapped energetic electrons and the wave, with the curves $\omega_{\text{precession}} - \omega = 0$ superposed for several values of ω, as obtained by the time evolution of a set of test particles.

The dependence of the mode frequency and growth rate of the e-fishbone on the magnetic field B_T, while keeping $\beta_{Ee,i}$ and $T_{Ee,i}$ constant, is shown in Fig. *7.*; note that $n_{Ee0}/n_{i0} = 0.2$ for those cases. Mode frequency scales approximately as $\omega/\omega_{A0} \propto 1/B_T^{1.5}$, somewhat weaker than expected from an analytical scaling (see [26], Eq.(9)) where only deeply trapped particles were considered ($\omega_{\text{theory}}/\omega_{A0} \simeq \overline{\omega}_{dEe}/\omega_{A0} \propto 1/B_T^2$, again assuming $\beta_{Ee,i}$ and $T_{Ee,i}$ to be constant; $\overline{\omega}_{dEe}$ is the bounce averaged precession frequency of the energetic electrons).

Although HMGC is a global code, and, thus, the frequency of a unstable mode being determined by the competitive effects of drive (in this case, due to energetic electrons) and damping (Alfvén continuum and ion Landau damping), Fig. *6.* shows that the precession frequency of the trapped energetic electrons being situated in a specific portion of the $(\hat{\mu}, \hat{u})$ plane plays a major role in determining the real frequency of the mode [25]. The specific localization of the maximum power exchange along the resonance curve in the plane $(\hat{\mu}, \hat{u})$ would result, in turn, from the de-

FIG. 7.: Mode frequency (open circles) and growth rate (full squares) vs. B_T for the e-fishbone.

tails of the energetic particles contribution (see, e.g., Eq. (7) of Ref. [26]). As a result, the mode behaviour in our numerical experiment, for testing the scaling of mode frequency and growth rate with B_T, is a compromise between the lowest order fishbone response, $\omega \simeq \overline{\omega}_{dEe}$, and the necessity of maximizing the drive $\gamma/\omega_{A0} \propto (B_T/B_0)^{3/4} \exp(-B_T^{1/2}/B_0^{1/2})$, with $B_0 = 5$T as reference. This scaling of γ/ω_{A0} fits well that of Fig. *7.* and is obtained readily from $\gamma/\omega \sim B_T E_{\text{res}}^{5/2} \exp(-E_{\text{res}}/T)$ [25, 26], given $E_{\text{res}} \sim (\omega B_T)$ the resonance energy for optimized wave-particle power exchange and the observed scaling for the real frequency
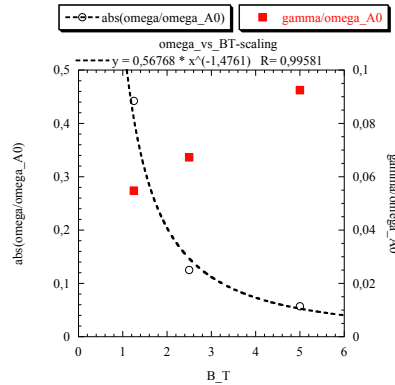
$\omega \propto B_T^{-1/2}$. The power exchange in the $(\hat{\mu}, \hat{u})$ plane is shown in Fig. 8.: the pattern does not change qualitatively, apart from the observation that the regions of highest power exchange move along the resonance curves toward higher energies, as expected from the frequency scaling, suggesting $\hat{\mu} \propto B_T^{-1/2}$.
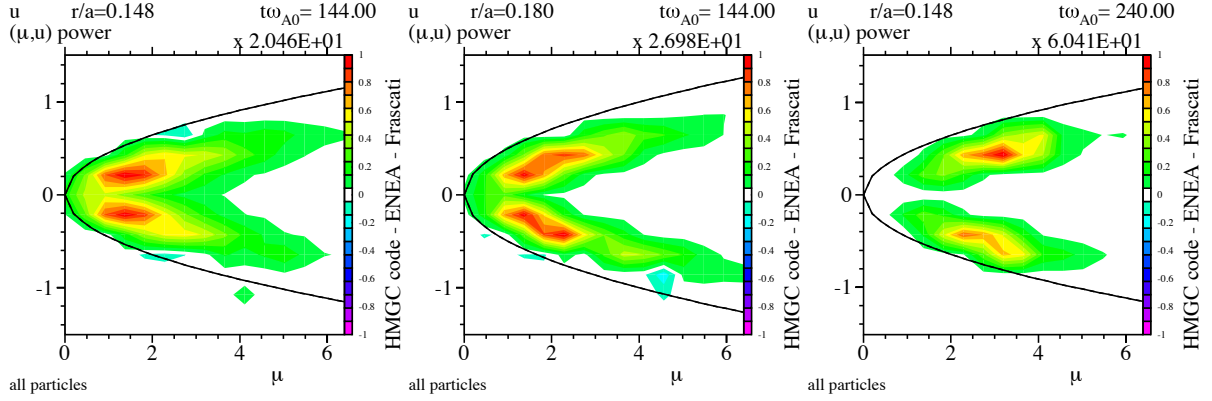

FIG. 8.: Power exchanges between energetic electrons and the wave for $B_T = 5$T (left), $B_T = 2.5$T (centre), and $B_T = 1.25$T (right), $n_{Ee0}/n_{i0} = 0.2$.

3. Benchmarks of HYMAGYC

HYMAGYC [19] is the new Hybrid Magnetohydrodynamic-Gyrokinetic code developed in Frascati, written in order to overcome some of the HMGC restrictions. Main characteristics of the code are: the thermal (core) plasma is described by full, resistive MHD linear equations in general curvilinear flux coordinates with arbitrary cross section (fluid nonlinearities are presently not retained); the MHD module provides e.m. potentials (vector potential **A** and electrostatic potential ϕ) required by the gyrokinetic module. As for the energetic-ion population, particle gyrocenter-coordinates are evolved by solving the gyrokinetic equations up to order $O(\epsilon^2)$ and $O(\epsilon\epsilon_B)$ (where $\epsilon \sim \rho_E/L_n$ is, here, the gyrokinetic ordering parameter, ρ_E being the ion Larmor radius of the energetic particle, L_n the equilibrium scale length and $\epsilon_B \sim \rho_E/L_B$, L_B being the equilibrium magnetic field scale length); the perturbed quantities satisfy the nonlinear gyrokinetic ordering [27] ($\omega/\Omega_{cE} \approx k_\parallel \rho_E = O(\epsilon)$, $k_\perp \rho_E = O(1)$). In this section, we present some validation tests that have been performed on the gyrokinetic module newly written for HYMAGYC. To this purpose, the particles response to assigned time varying e.m. fields computed by HYMAGYC has been compared with an analytical solution and with the solution provided by HMGC. The analytical solution, which is well in the limit of validity also of HMGC, has been derived assuming circular, concentric magnetic surfaces, small inverse aspect ratio $\epsilon \equiv a/R_0 = 0.01$, uniform safety factor profile, and small Larmor gyroradius $\rho_E/a = 0.01$. Moreover, only the parallel (to the equilibrium magnetic field) component of the vector potential and the electrostatic potential have been considered, with assigned real frequency and growth-rate, and a single Fourier component:

$$\phi^{(m,n)}(r,t) = \phi_0(r/a)^m e^{-\left(\frac{r-r_0}{\Delta_0}\right)^2} e^{-i\omega t}, \tag{4}$$

$$A_\parallel^{(m,n)}(r,t) = A_{\parallel,0}(r/a)^m e^{-\left(\frac{r-r_1}{\Delta_1}\right)^2} e^{-i\omega t} \tag{5}$$

with $m = n = 4$, $\phi_0 = A_{\parallel,0} = 10^{-10}$, $r_0/a = 0.3$, $r_1/a = 0.6$, $\Delta_0/a = \Delta_1/a = 0.2$, $\omega/\omega_{A0} = (0.3 + i0.01)$. The distribution function for the energetic particles is bi-Maxwellian with uniform radial profiles and $T_{E,\perp}/T_{E,\parallel} = 0.01$ and a normalized density profile $n_E(r)/n_{E0} =$
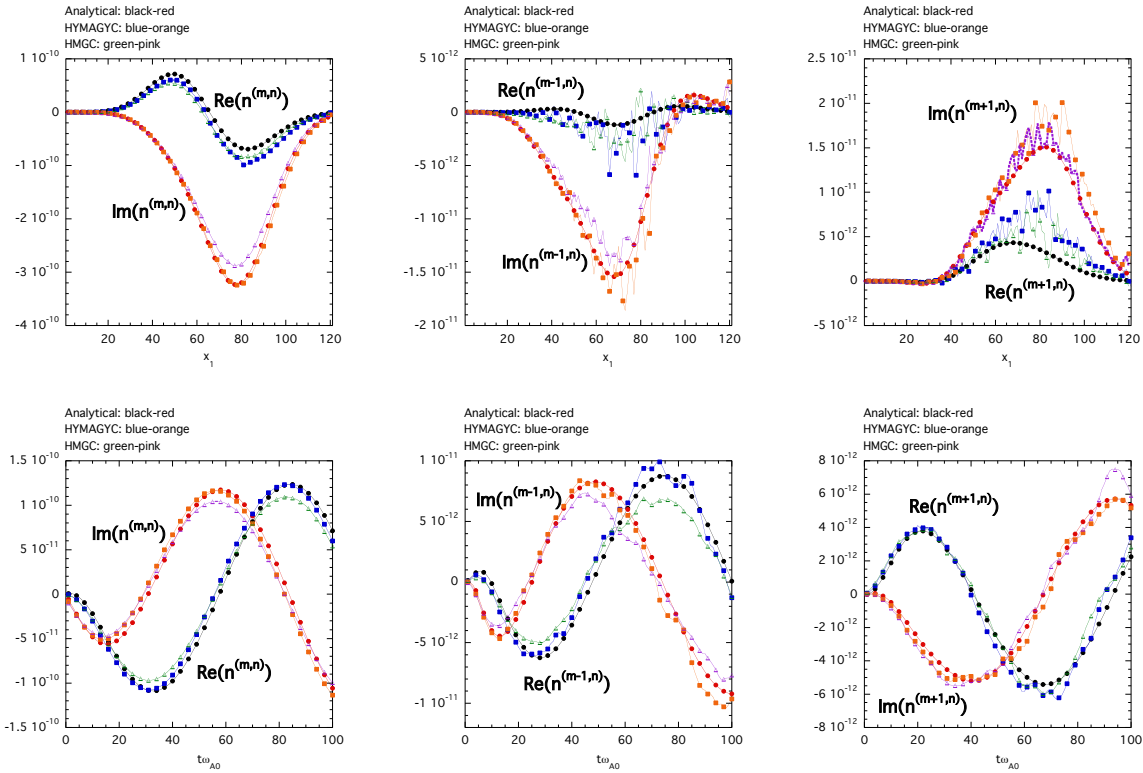
FIG. 9.: Perturbed density response (real and imaginary contributions) of the driven $(m, n) = (4, 4)$ component and those of the first satellites $(m \pm 1, n)$ are shown: radial profiles at a specific time (top; the abscissa is the array index of the radial coordinate x_1, "1" corresponding to the axis and "121" to the plasma surface), and time evolution at normalized radial coordinate $x_1 = 0.5$.

$\exp^{-2.5(r/a)^2}$. The analytical derivation follows the one obtained in Ref. [2], and has been obtained by neglecting the mirroring term in the parallel velocity equation of motion, and considering only unperturbed particles motion. A comparison between the analytical solution and the results obtained by HMGC and HYMAGYC is shown in Figs. 9., where the perturbed density response of the driven $(m = 4, n = 4)$ component and those of the first satellites $(m \pm 1, n)$ are reported (note that the amplitudes of the satellites are much lower than the one the driving component, thus justifying the higher noise observed).

References

[1] W. Park, S. Parker, H. Biglari, M. Chance, L. Chen, C.Z. Cheng, T.S. Hahm, W.W. Lee, R. Kulsrud, D. Monticello, L. Sugiyama, and R.B. White, *Phys. Fluids B*, **4**, (1992) 2033.

[2] S. Briguglio, G. Vlad, F. Zonca, and C. Kar, *Phys. Plasmas*, **2**, (1995) 3711.

[3] S. Briguglio, F. Zonca, and G. Vlad, *Physics of Plasmas*, **5**, (1998) 3287–3301.

[4] S. Briguglio, G. Vlad, F. Zonca, and G. Fogaccia, *Physics Letters A*, **302**, (2002) 308–312.

[5] F. Zonca, S. Briguglio, L. Chen, S. Dettrick, G. Fogaccia, D. Testa, and G. Vlad, *Physics of Plasmas*, **9** (2002) 4939–4956.

[6] G. Vlad, S. Briguglio, G. Fogaccia, and F. Zonca, *Plasma Physics and Controlled Fusion*, 46, (2004) S81–S93.

[7] W. Park, E.V. Belova, G.Y. Fu, X.Z. Tang, H.R. Strauss, and L.E. Sugiyama, *Phys. Plasmas*, **6**, (1999) 1796.

[8] G.Y. Fu, W. Park, H.R. Strauss, J. Breslau, J. Chen, S. Jardin, and L.E. Sugiyama, *Phys. Plasmas*, **13**, (2006) 052517.

[9] Y. Todo and T. Sato, *Phys. Plasmas*, **5**, (1998) 1321.

[10] Y. Todo, K. Shinohara, M. Takechi, and M. Ishikawa, *Phys. Plasmas*, **12**, (2005) 012503.

[11] Y. Todo, *Phys. Plasmas*, **13**, (2006) 082503.

[12] S. Briguglio, G. Fogaccia, G. Vlad, F. Zonca, K. Shinohara, M. Ishikawa, and M. Takechi, *Physics of Plasmas*, **14**, (2007) 055904.

[13] G. Vlad, S. Briguglio, G. Fogaccia, F. Zonca, C. Di Troia, W.W. Heidbrink, M.A. Van Zeeland, A. Bierwage, and X. Wang, *Nuclear Fusion*, 49:075024, 2009.

[14] G. Vlad, S. Briguglio, G. Fogaccia, F. Zonca, and M. Schneider, *Nuclear Fusion*, **46** (2006) 1–16.

[15] A. Cardinali, M. Baruzzo, C. Di Troia, M. Marinucci, A. Bierwage, G. Breyiannis, S. Briguglio, G. Fogaccia, G. Vlad, X. Wang, F. Zonca, V. Basiuk, R. Bilato, M. Brambilla, F. Imbeaux, S. Podda, and M. Schneider, Energetic particle physics in FAST H-mode scenario with combined NNBI and ICRH, In *Fusion Energy 2010*, Vienna, 2010, Paper THW/P7-04. International Atomic Energy Agency.

[16] X. Wang, S. Briguglio, L. Chen, G. Fogaccia, G. Vlad, and F. Zonca, *Physics of Plasmas*, **18**, (2011) 052504.

[17] K. Shinohara, T. Kurki-Suonio, D. Spong, O. Asunta, K. Tani, E. Strumberger, S. Briguglio, T. Koskela, G. Vlad, S. Günter, G. Kramer, S. Putvinski, K. Hamamatsu, and ITPA Topical Group on Energetic Particles, *Nucl. Fusion*, **51**, (2011) 063028.

[18] L. Chen, Z. Lin, W. Deng, D. Spong, G.Y. Sun, X. Wang, W.L. Zhang, A. Bierwage, S. Briguglio, I. Holod, G. Vlad, Y. Xiao, and F. Zonca, Verification of gyrokinetic particle simulation of Alfvén eigenmodes excited by external antenna and by fast ions, In *Fusion Energy 2010*, Vienna, 2010, Paper THW/P7-05. International Atomic Energy Agency.

[19] G. Vlad, S. Briguglio, G. Fogaccia, and F. Zonca, Toward a new hybrid MHD gyrokinetic code: Progresses and perspectives. In *11th IAEA Technical Meeting on Energetic Particles in Magnetic Confinement Systems, Kyiv 21-23 Sept. 2009*, pages P–25, Vienna, Austria, 2009. International Atomic Energy Agency.

[20] K.L. Wong et al., *Phys. Rev. Lett.* **85** (2000) 996.

[21] M. Valovic et al., *Nucl. Fusion* **40** (2000) 1569.

[22] X.T. Ding et al., *Nucl. Fusion* **42** (2002) 491.

[23] P. Smeulders et al., Fast MHD Analysis on FTU. In *Proc. 29th EPS Conf. on Plasma Physics Controlled Fusion (Montreux, Switzerland, 2002*, vol 26B (ECA) D-5.016 and http://epsppd.epfl.ch/Montreux/start.htm.

[24] P. Maget et al., *Nucl. Fusion* **46** (2006) 797.

[25] F. Zonca et al., *Nucl. Fusion* **47** (2007) 1588–1597.

[26] F. Zonca et al., *Nucl. Fusion* **49** (2009) 085009.

[27] E.A. Frieman and Liu Chen, *Phys. Fluids* **23** (1982) 502.